Study on the promotional effect of lanthana addition on the performance of hydroxyapatite-supported Ni catalysts for the CO_2 methanation reaction

Zouhair Boukha [*], Alejandro Bermejo-López, Beñat Pereda-Ayo, José A. González-Marcos, Juan R. González-Velasco

Chemical Technologies for Environmental Sustainability Group, Department of Chemical Engineering, Faculty of Science and Technology, University of the Basque Country UPV/EHU, P.O. Box 644, E-48080 Bilbao, Spain

ARTICLE INFO

ABSTRACT

The performance of nickel supported on lanthana-modified hydroxyapatite (HAP) catalysts is investigated in the CO_2 methanation. The addition of La (1–6.6 wt%) leads to a surface enrichment following a sequential multilayer deposition model. Moreover, La addition systematically improves the dispersion of Ni particles and their reducibility, which in turn increases spectacularly the amounts of basic sites and their thermal stability. Such physicochemical changes impact positively on the activity of the catalysts in CO_2 methanation. The estimated turnover frequency (TOF) suggest that the small Ni particles are the most efficient. The latter seem to provide a large density of very active defects on Ni-La_2O_3 interface. The optimized catalyst proves to be highly resistant to deactivation during 100 h time-on-stream (TOS). The samples were also assayed as dual function materials (DFMs) for CO_2 adsorption and methanation. A scheme is proposed to describe the different steps involved in a CO_2 adsorption/hydrogenation cycle.

1. Introduction

Nowadays, global warming is one of the most debated environmental problems which requires immediate actions to mitigate the resulting damage posing a serious threat to the ecosystems [1–5]. This is actually a direct consequence of the abundant emissions of carbon dioxide, considered as the main greenhouse gas (GHG). Due to its high activity in trapping radiation, as well as the continuous increase in its production, it has been proved that CO_2 emission causes a systematic increase in global temperature. Therefore, the international community is currently strongly promoting strategies for reducing the current global CO_2 emissions (> 410 ppm) to acceptable levels (< 350 ppm) [1]. To overcome these issues considerable efforts have been devoted to develop efficient and clean energy technologies based on the re-utilization of CO_2 captured from industrial waste gases, as one of the most viable solutions [2–7]. In this sense, the reaction of CO_2 with renewable hydrogen to produce synthetic natural gas (SNG), through the *Sabatier* reaction is an attractive strategy allowing the implementation of *Power-to-Gas* technology [6,7]. The feasibility of this strategy can also be justified by the availability of the SNG storage and transport facilities. The CO_2 methanation reaction is a catalytic process, where the use of active materials is essential. Though a number of reports dealing with different class of transition metal catalysts are presently available, due to their high activity supported Ru and Ni catalysts are by far the most investigated ones [2–5]. Regarding economic considerations, Ni catalysts have attracted a special attention. However, a number of drawbacks strongly restrict their application, since they present high susceptibility to sintering and/or coke deposition and consequently a deactivation/loss of the active sites [8]. To address this issue, numerous formulations have been investigated to improve the dispersion and sintering-resistance of Ni particles. In this sense, the nature of the catalyst support plays a crucial role in the distribution and the stability of the Ni active phases. For this reason, the design of Ni catalysts exhibiting suitable metal-support interactions is essential. There is a wide consensus on the bi-functionality of the CO_2 methanation mechanism, where the activation of H_2 occurs on the metallic Ni, while CO_2 is activated on the chemically active support surface [9–14]. Thus, due to the acidic character of the CO_2 molecule, its activation is rather favoured on surface basic sites. Usually, Ni active phases are supported on metal oxides presenting relatively high specific surface area, including Al_2O_3, SiO_2 and zeolites, among others. Their surface chemistry can be modified by addition of CO_2 adsorbents mainly consisting of alkali metals (e.

g. Na^+ and K^+), alkaline earth metals (e.g. Ca^{2+}, Ba^{2+}, Mg^{2+}, Sr^{2+}) and rare earth sesquioxides (Ln_2O_3) [2–5,8–13,15,16].

It is known that lanthana is the member of the Ln_2O_3 family exhibiting the highest basicity, thus becoming an interesting candidate for processes catalyzed by basic materials [17]. Though the positive impact of La addition on Ni activity was already evidenced, the nature of the used support can influence the properties of both La and Ni supported species [8,11–13]. Quindimil et al. [8] studied the influence of La addition on the performance of Ni/zeolite catalysts in the CO_2 methanation reaction. Their H_2-TPR data revealed that progressive addition of La decreased the reducibility of prepared catalysts. Nevertheless, the presence of La markedly improved the catalytic activity, achieving CO_2 conversion values close to thermodynamic equilibrium at 450 °C, owing to the significant increase in the density of surface basic centres (composed of weak and strong sites) as well as the improvement of the dispersion of Ni active sites. However, the stability test of their optimized formulation at 350 °C showed that CO_2 conversion decreased from 70% to 60% in the initial 24 h. The positive effect of La promoter (4–37 wt%) on the activity of Ni/Al_2O_3 catalysts was reported by Garbarino et al. [12]. They observed that the presence of La hinders the reduction of the catalysts. Moreover, kinetic data showed that addition of La increased the hydrogen order while it lowered the CO_2 reaction order. They attributed the promoter effect of La to its strong basicity which allowed the formation of active surface carbonates acting as "reactant reservoirs". Wierzbicki et al. [11] prepared La-promoted Ni-Mg-Al hydrotalcite-derived catalysts by co-precipitation method. They reported that the introduction of La affected the distribution of the surface basicity, generating medium-strength basic sites, and enhanced the reducibility of Ni species, by weakening the Ni-hydrotalcite interactions. In their study on a series of Ni supported on CeO_2 catalysts, Siakavelas et al. [18] found that the simultaneous incorporation of La^{3+} and Pr^{3+} (or La^{3+} and Sm^{3+}) markedly increased the density of ceria oxygen vacant sites. In addition, irrespective of the second promoter added (Mg^{2+}, Pr^{3+} or Sm^{3+}), the presence of La^{3+} increased the amounts of medium-strength basic sites, which positively impacted the performance of the catalysts in the CO_2 methanation reaction.

On the other hand, catalysis by transition metals stabilized on HAP materials has attracted an increased interest in the last decades [19–27]. Previous reports pointed out that over HAP-based catalysts high performances could be achieved in a variety of catalytic reactions, including CO_2 methanation and demanding processes such as CO_2 reforming of methane [21–23]. This was attributed to the advantageous chemical and physical properties of HAP, making it a promising catalyst support. In addition, the surface chemistry of HAP can be tuned by varying the Ca/P atomic ratio and/or the ion-exchange with a wide number of cations and anions.

In the present work we investigate, for the first time, to our knowledge, the promotional effect of lanthanum addition on the catalytic properties of a Ni/HAP system in the CO_2 methanation reaction. A stoichiometric HAP carrier was synthesized by co-precipitation method and subsequently impregnated with La and Ni. The resulting catalysts were then characterized by a wide battery of complementary techniques, including BET, XRD, H_2-TPR, CO_2-TPD, HAADF-X EDS and XPS spectroscopy. The improved catalytic properties of the lanthana promoted samples were linked to the occurrence of suitable surface chemistry and the dispersion of the Ni active phase.

2. Experimental

2.1. Preparation of the catalysts

The HAP support (Ca/P = 1.67) was synthesized by co-precipitation using two aqueous solutions containing $Ca(NO_3)_2.4 H_2O$ (1 mol L^{-1}) and $(NH_4)_2HPO_4$ (0.6 mol L^{-1}) salts, at 80 °C. The pH of the suspension was adjusted to about 10 by using ammonia solution. After stirring for 16 h, the recovered solid was washed with distilled water, until reaching pH 7,

and then dried at 120 °C for 12 h. The resulting HAP sample was finally heat treated in air at 500 °C for 4 h.

Ni/La-(x) catalysts were prepared by modification of the HAP support with La and Ni precursors, subsequently. First, three La doped HAP samples were prepared by impregnation, using solutions with three different amounts of the $La(NO_3)_3.6H_2O$ salt. The resulting samples, La-(x), were dried at 120 ºC for 12 h, and then calcined for 4 h at 500 °C. Finally, the Ni/La-(x) catalysts were prepared by impregnation of the synthesized HAP and the three La-modified HAP samples from aqueous solutions containing equal amount of Ni acetate tetrahydrate (Sigma-Aldrich, 98%) solution to achieve a nominal Ni loading equal to 3.3 wt %. Note that the latter had been previously optimized through testing monometallic Ni/HAP samples with different Ni loadings in the CO_2 methanation reaction. The resulting Ni/La-(x) samples were dried at 120 °C, for 12 h, and then calcined in air at 500 °C for 4 h.

2.2. Characterization techniques

The actual contents of Ca, P, La and Ni were determined by means of inductively coupled plasma atomic emission spectroscopy (ICP-AES).

The textural properties of the activated catalysts were investigated by N_2 physisorption experiments at − 196 °C on a Micromeritics (TRISTAR II 3020) apparatus. The samples were heat-treated at 300 °C under N_2 flow (50 cm^3 min^{-1}, STP) for 8 h.

The X-ray diffraction (XRD) analyses were conducted at room temperature on a X'PERT-MPD X-ray diffractometer using Cu Kα radiation.

The X-ray photoelectron spectroscopy (XPS) surface analyses for the Ni/La(x) samples were performed on a SPECS apparatus equipped with Phoibos 150 1D-DLD analyzer and monochromatic Al Kα radiation (1486.6 eV). The conductivity of the samples was improved using an electron flood gun. To correct the charging effects, the C 1 s core level was used as a reference (284.6 eV). The analyses were performed on samples pre-reduced in-situ at 500 °C for 1 h (under a 20% H_2/Ar flow). For this pre-treatment we used a high-temperature cell (HT SPECS) allowing thermal treatments under controlled atmospheres.

The distribution of Ca, P, La and Ni elements for the reduced Ni/La-(x) samples were investigated by combining high-angle annular dark field (HAADF) with X-ray energy dispersive spectroscopy (X-EDS) techniques. For these studies, we used a high-performance microscope FEI Titan Cubed G2 60–300 working at 300 kV. The equipment also includes a monochromator, a Schottky X-FEG field emission electron gun, a CEOS GmbH spherical aberration (Cs) corrector and a Super-X EDX system for Z contrast imaging in STEM conditions.

The temperature programmed reduction with H_2 (H_2-TPR) experiments were carried out on a Micromeritics AutoChem 2920 apparatus. The samples were cleaned in a flow of 5% O_2/He at 500 °C for 60 min and then cooled to 50 °C in He. Finally, they were reduced under 5% H_2/Ar gas flow (50 cm^3 min^{-1}, STP) by increasing the temperature with a ramp of 10 °C min^{-1} from 50 to 550 °C.

The temperature programmed desorption of CO_2 (CO_2-TPD) experiments were performed on an AutoChem 2920 instrument (Micromeritics) coupled to a mass spectrometer (Hiden Analytical). The samples (60 mg) were pre-treated in 5% H_2/Ar flow at 500 °C for 1 h. The adsorption of CO_2 (at 50 °C) was performed submitting the samples to a flow of 5% CO_2/He for 30 min. After CO_2 adsorption they were treated with He for 1 h and then heated at 10 °C min^{-1} to 800 °C.

The temperature programmed surface reaction (TPSR) experiments were performed using the same equipment used for CO_2-TPD. The sample (60 mg) was pre-reduced under 5% H_2/Ar at 500 °C for 1 h, and then cooled down to 100 °C. Subsequently, it was exposed to a flow of 5% CO_2/He (50 cm^3 min^{-1}, STP) for 20 min. After switching to a 5% H_2/Ar gas flow (50 cm^3 min^{-1}, STP) the sample was held at 100 °C for 20 min, and finally heated from 100 to 800 °C with a ramp of 10 °C min^{-1}. The active fraction of basic sites (f_{ABS}) was determined according to the following expression:

$$f_{ABS}(\%) = \frac{n_{CH4}^{TPSR}}{n_{CO2}^{TPD}} \times 100 \tag{1}$$

where n_{CH4}^{TPSR} represents the amounts of produced CH_4 (mol_{CH4} g^{-1}) during the TPSR experiments and n_{CO2}^{TPD} represents the total amounts of desorbed CO_2 (mol_{CO2} g^{-1}) during the CO_2-TPD experiments.

In order to evaluate the coke deposition on the Ni/La-(6.6) catalyst, submitted to the CO_2 methanation reaction at 350 °C for 100 h TOS, thermogravimetric analysis (TGA) experiments were performed in oxidative atmosphere. These experiments were carried out with a Setaram Setsys Evolution thermobalance under atmospheric pressure. The sample (50 mg) was first dried in synthetic air (50 cm^3 min^{-1}, STP) at 120 °C for 1 h and then heated to 1000 °C (10 °C min^{-1}).

2.3. Catalytic performance testing

2.3.1. CO2 methanation experiments

The experiments corresponding to the CO_2 methanation reaction were performed in a tubular flow reactor (ID = 9 mm) working at atmospheric pressure. The pre-treatment of the catalysts consisted of their reduction at 500 °C under a 20% H_2/He flow (100 cm^3 min^{-1}, STP) for 1 h and cooling to 200 °C in a flow of He. The reaction mixture was composed of 16% CO_2, 64% H_2 and 20% He. The experiments were carried out using 250 mg of catalyst (160–250 μm) diluted with quartz (V_{bed} = 1.5 cm^3) and a total flow of 125 cm^3 min^{-1} (STP), which corresponds to a WHSV of 30,000 cm^3 g^{-1} h^{-1}. The reaction temperature was sequentially increased, with intervals of 25 °C, from 200 to 500 °C.

The analysis system consisted of a Gas Chromatograph (Agilent Technologies 490 Micro GC) equipped with a TCD detector. Note that the mass balance was assessed by calculation of the difference between the total amounts of inlet and outlet carbon-containing molecules (CO_2, CH_4 and CO). The values of CO_2 conversion (X_{CO2}) and selectivity to CH_4 (S_{CH4}) and CO (S_{CO}) were calculated according to the following expressions:

$$X_{CO2} = \frac{F_{CO2}^{in} - F_{CO2}^{out}}{F_{CO2}^{in}} \times 100 \tag{2}$$

$$S_{CH4} = \frac{F_{CH4}^{out}}{F_{CO2}^{in} - F_{CO2}^{out}} \times 100 \tag{3}$$

$$S_{CO} = \frac{F_{CO}^{out}}{F_{CO2}^{in} - F_{CO2}^{out}} \times 100 \tag{4}$$

where F_i^{in} and F_i^{out} are the inlet and outlet molar flows, respectively, of a gas molecule "i".

2.3.2. Cyclic tests of CO2 adsorption and methanation

The investigated Ni/La-(x) samples were also assayed as DFMs for CO_2 adsorption and methanation. Their performance under CO_2 storage/reduction cycle conditions was evaluated in a tubular reactor operating at atmospheric pressure. Prior to their testing, the samples (1 g) sieved to 300–500 μm were reduced under 10% H_2/Ar at 500 °C for 1 h. After cooling to 280 °C, under flowing Ar, a series of CO_2 storage/reduction cycles were carried out in the temperature range of 280–520 °C, according to the procedures reported elsewhere [28–30]. For each cycle four consecutive steps were performed under a total flow of 1200 cm^3 min^{-1} (STP): (i) CO_2 adsorption period for 1 min, using a 10% CO_2/Ar flow, (ii) Ar purging for 2 min to remove weakly adsorbed CO_2, (iii) hydrogenation period for 2 min, using a 10% H_2/Ar flow and (iv) purging with Ar for 1 min. The composition of the gas mixtures (CO_2, CH_4, CO and H_2O) was analyzed using a MultiGas 2030 FTIR analyzer. The amounts of CO_2 stored for a time (t) and the produced amounts of CH_4 and CO, respectively, were calculated according the following equations:

$$Stored CO_2 (\mu mol \quad g^{-1}) = \frac{1}{W} \int_0^t [F_{CO2}^{in}(t) - F_{CO2}^{out}(t)] dt \tag{5}$$

$$Y_{CH4} (\mu mol \quad g^{-1}) = \frac{1}{W} \int_0^t F_{CH4}^{out}(t) \quad dt \tag{6}$$

$$Y_{CO} (\mu mol \quad g^{-1}) = \frac{1}{W} \int_0^t F_{CO}^{out}(t) \quad dt \tag{7}$$

where W is the DFM weight.

3. Results and discussion

3.1. Characterization

3.1.1. Textural properties

The N_2 adsorption/desorption isotherms and the distribution of the pore sizes for the Ni/La-(x) samples are included as Supplementary material (Fig. S1 and Fig. S2, respectively). It can be observed that the analyzed samples exhibit a similar shape of their corresponding isotherms and hysteresis loops (Fig. S1). Furthermore, according to their resulting pore size distribution, presenting maxima centered between 30 and 35 nm, all analyzed samples may be considered as mesoporous materials (Fig. S2). Table 1 summarizes the textural properties of the reduced Ni/La-(x) catalysts. In contrast to the samples with low La loadings (1% and 3.7%), the addition of 6.6 wt% La induces a significant loss in the BET surface area, from 53 m^2 g^{-1} for Ni/La-(0), to 45 m^2 g^{-1} for Ni/La-(6.6).

3.1.2. HAADF and nano-analytical studies

The activated Ni/La-(x) samples were also investigated by combining HAADF and X-EDS techniques. Since the resulting contrasts depend on the atomic number, these techniques are particularly suitable for a simultaneous nano-analysis of both light and heavy elements, providing their spatial distribution in deeper detail. Fig. 1(a-d) displays the HAADF image and the X-EDS maps corresponding to Ca, P and Ni elements, respectively, spread on the monometallic sample (Ni/La-(0)). Expectedly, the major constituents of the HAP support (Ca and P) present a homogeneous distribution (Fig. 1b and c). By contrast, as shown in Fig. 1d, the Ni map clearly indicates the concentration of metallic Ni in many localized nano-regions of the sample (sparkling particles). Fig. 2 (a-i) show the HAADF images and the maps corresponding to La and Ni elements for the La-modified samples. In consistency with the XRD data (will be commented below), the La map for the Ni/La-(1) sample reveals that lanthanum is homogeneously dispersed (Fig. 2b). However, at higher contents, analyzed zones exhibiting La-rich domains are clearly observed, but not to the extent of the occurrence of a tridimensional growth of La species nano-crystallites (Fig. 2e and h). As expected, this effect is more pronounced on the sample with the highest La loading (6.6 wt%) (Fig. 2h), which is consistent with the presence of a relatively large surface density of lanthanum (6.4 La^{3+} nm^{-2}) compared with that required for the formation of a theoretical monolayer (5.4 La^{3+} nm^{-2}) [17,19]. On the other hand, it seems that the distribution of the Ni particle size spread on the series of the catalysts depends on La content. The monometallic sample exhibits the widest distribution and the largest Ni particles with an average diameter close to 15.3 nm (Fig. 2j and Table 1). Interestingly, the progressive addition of La significantly decreases the Ni particles size from 15.3 nm (Ni/La-(0)) to 10.3 nm for Ni/La-(1), 8.2 nm for Ni/La-(3.7), and 8.1 nm for Ni/La-(6.6). A similar tendency was observed in a previous study on Ni/La/zeolite catalysts [8]. This positive effect of La addition on the dispersion of Ni particles was linked to the occurrence of suitable interactions, probably inherent to a synergistic effect in the interface between metallic Ni and La species.

Table 1
ICP, BET, XRD and HAADF data for the reduced Ni/La-(x) samples.

| Sample	ICP			BET			XRD		HAADF	
	Ca/P	Ni, %	La, %	S_{BET}, $m^2\,g^{-1}$	V_p, $cm^3\,g^{-1}$	d_p, nm	d_{HAP}, nm	d_{Ni}, nm	d_{Ni}, nm	D_{Ni}; %
HAP	1.65	0	0	55	0.41	27.7	43.9	–	–	–
Ni/La-(0)	1.64	3.3	0	53	0.37	26	43.0	16.2	15.3	8.1
Ni/La-(1)	1.65	3.2	1	51	0.38	27.5	42.6	14.4	10.3	12.1
Ni/La-(3.7)	1.63	3.3	3.7	53	0.34	23.1	43.8	13.7	8.2	15.1
Ni/La-(6.6)	1.66	3.2	6.6	45	0.31	24.7	45.8	15.3	8.1	15.3
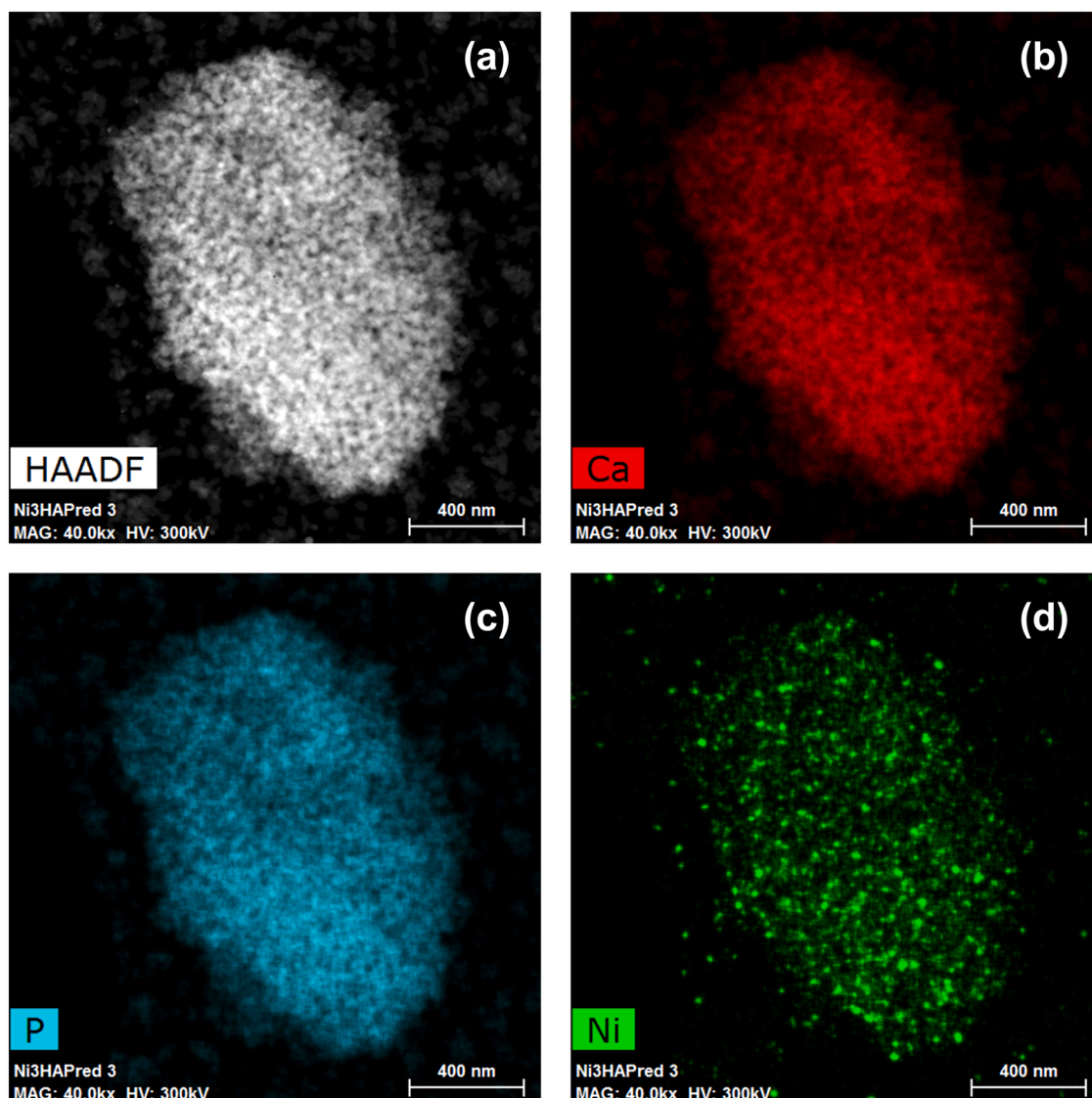
Fig. 1. (a) HAADF image for the reduced Ni/La-(0) catalyst and (b, c, and d) images displaying the color maps for Ca, P and Ni, respectively, given by X-EDS analysis.

3.1.3. Macro-structural studies

Fig. 3a and b displays the XRD patterns for the HAP bare support and the Ni/La-(x) post-reduction catalysts. The diffractogram of the HAP sample evidences the formation of a unique crystalline phase identical to that of the apatite structure, belonging to the $P6_3/m$ space group (JCPDS: 01–082–256). Moreover, the deposition of both Ni and La does not affect the position of the characteristic diffraction peaks of HAP. The patterns of the Ni/La-(x) post-reduction samples show that Ni species are completely reduced into metallic Ni (JCPDS: 89–7120), but no diffraction peak due to La species can be observed. It should be noted that by means of HAADF techniques, besides the highly dispersed La species,

some La-rich domains have also been detected. We think that the absence of the latter from the XRD patterns is probably due to their low crystallinity.

A careful analysis of the metallic Ni diffraction peak broadness was made in order to estimate the mean Ni particle size by Scherrer equation (Fig. 3b). Unexpectedly, as deduced from data of Table 1, the La-modified samples exhibit overestimated values when compared with those given by HAADF-X EDS data, which may be attributed to the occurrence of a strain broadening effect [24,31,32]. Interestingly, according to the dependence of the $d_{Ni}^{XRD}/d_{Ni}^{HAADF}$ ratio on the La loading, displayed in Fig. 3c, the observed tendency would imply an increase in
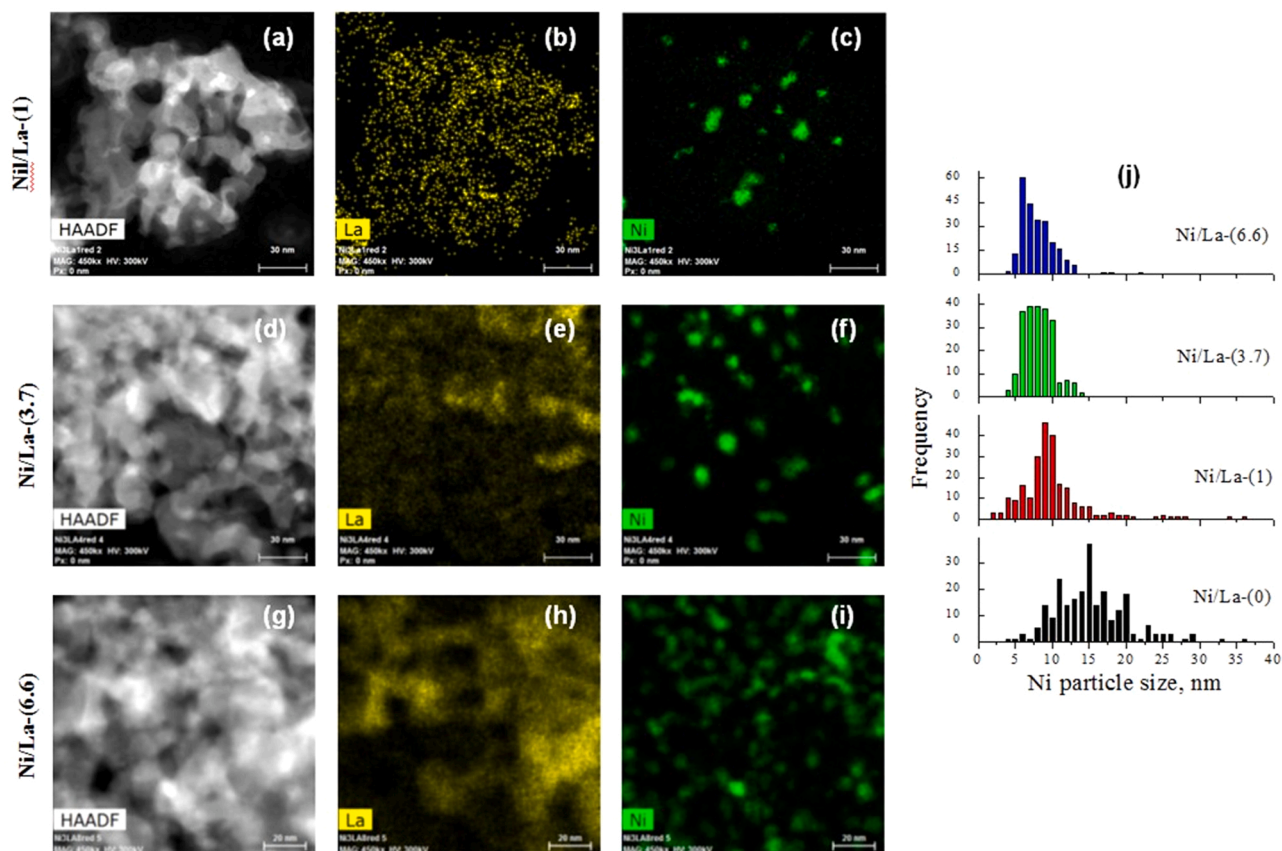
Fig. 2. HAADF images and the corresponding color maps for La and Ni, given by X-EDS, for the reduced samples: (a, b and c) Ni/La-(1), (d, e and f) Ni/La-(3.7) and (g, h and i) Ni/La-(6.6). (j) Profiles of the Ni particle sizes distribution.
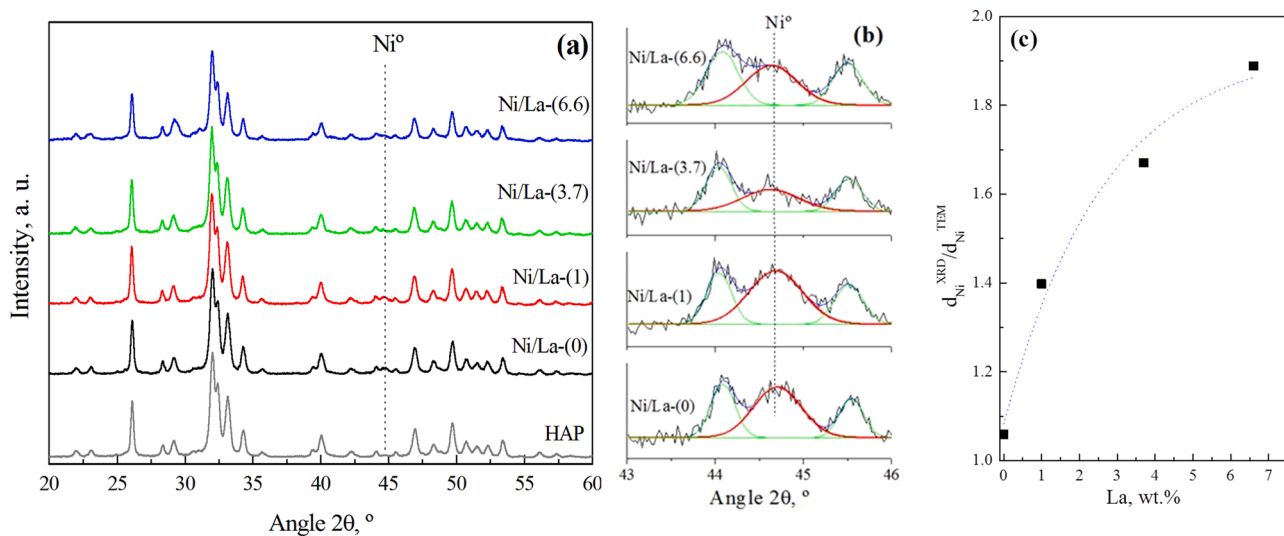
Fig. 3. (a) XRD patterns for the reduced Ni/La-(x) catalysts and (b) their zoom in the 2θ angle range of 43–46 °. (c) Dependence of d_{Ni}^{XRD} to d_{Ni}^{HAADF} ratio on the La loading.
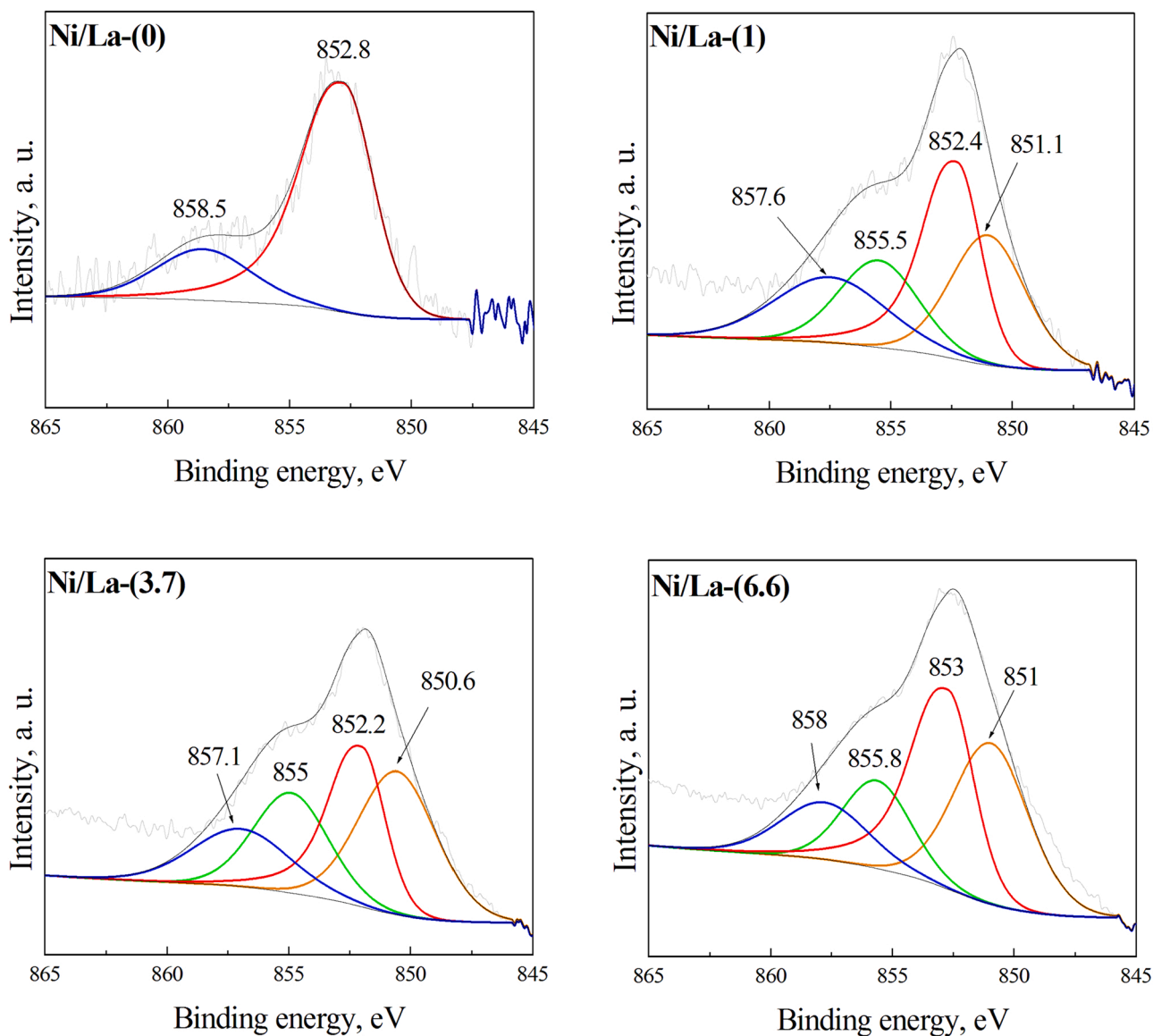
Fig. 4. XPS spectra recorded in Ni 2p$_{3/2}$ region of the reduced Ni/La-(x) catalysts.

Table 2
XPS data for the reduced Ni/La-(x) samples.

Catalyst	XPS						
	Ni 2p$_{3/2}$, eV	La 3d$_{5/2}$, eV	FWHM La 3d$_{5/2}$, eV	ΔE $_{(La\ 3d5/2)}$, eV [a]	Ni/P [b]	La/P	Ca/P
Ni/La-(0)	852.8 (858.5)[c]	–	–	–	0.04	0	1.61
Ni/La-(1)	852.3 (857.5)	835.5 (839.0)	3.58	3.5	0.08	0.051	1.56
Ni/La-(3.7)	852.0 (857.0)	834.8 (838.4)	3.89	3.6	0.11	0.092	1.56
Ni/La-(6.6)	852.7 (857.8)	835.1 (839.0)	4.53	3.9	0.21	0.161	1.59

[a] Satellite energy separation for the La 3d$_{5/2}$ region.
[b] Values corresponding to Ni/P atomic ratio.
[c] Values corresponding to satellite peak.

the density of Ni lattice imperfections with the La loading increase.

3.1.4. X-ray photoelectron spectroscopy (XPS) studies

The influence of La loading on the surface distribution of Ni and La on the reduced Ni/La-(x) catalysts has also been investigated by means of XPS. Fig. 4, Fig. S3 and Table 2 summarize the corresponding results. As deduced from data reported in Fig. S3 and Table 2, the La $3d_{5/2}$ spectra for the La-modified samples are characterized by the presence of a main photoemission peak and the corresponding satellite, centered at 835.1 ± 0.4 eV and 838.7 ± 0.3 eV, respectively, which can be assigned to the presence of La^{3+} ions forming La_2O_3 species [17,19]. Moreover, the broadness of the main peak increases with La content, which is probably due to an increase in the heterogeneity of its chemical environment [17]. Although not detectable by XRD, this tendency suggests a probable evolution in the structural nature of lanthana. Upon integration of the La $3d_{5/2}$ and P 2p spectra, the corresponding La/P atomic ratios could also be estimated. As deduced from Table 2, this ratio systematically increases with the progressive addition of La. In accordance with earlier studies [17,24] and our HAADF results, this behavior mainly indicates that there is no apparent segregation of lanthanum phases in the range of La loadings used in this work (1–6.6 wt%). Thus, we suggest that the surface enrichment of Ni/La-(x) catalysts with lanthanum is rather a stepwise process, following a multilayer deposition model. This conclusion is also supported by the estimated difference of BE between the main La $3d_{5/2}$ peak and its satellite, with values ranging from 3.5 eV to 3.9 eV, Table 2, when compared with 4.8 eV reported for bulk La_2O_3 [17].
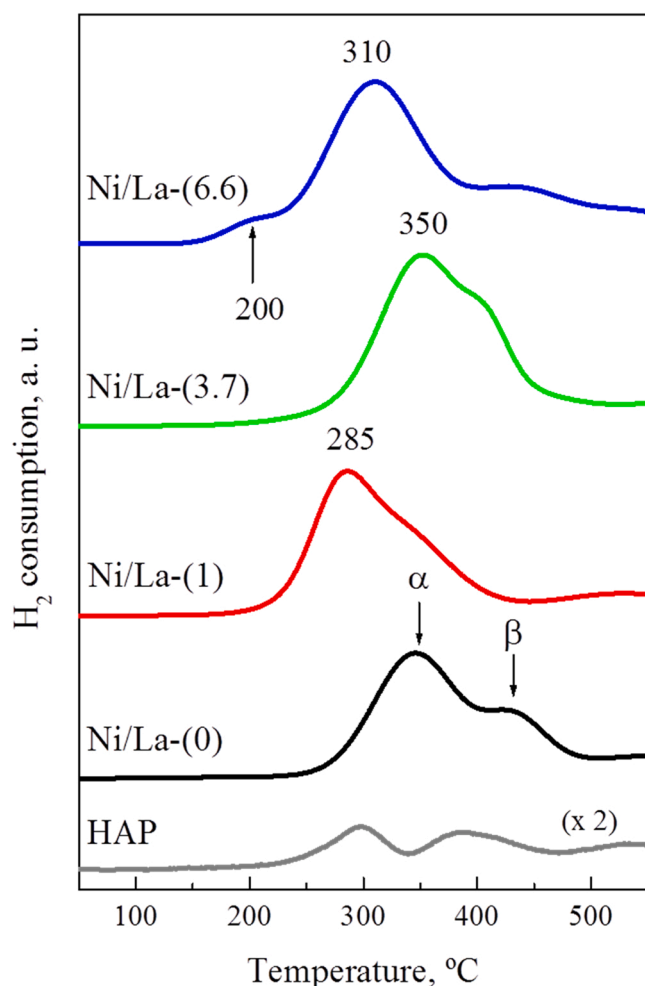

Fig. 5. H$_2$-TPR profiles for the Ni/La-(x) catalysts.

Fig. 4 displays the XPS spectra recorded in the Ni $2p_{3/2}$ region. For the Ni phase identification, the spectra were deconvoluted taking into account the constraints of equal spin-orbit splitting for Ni 2p peaks, keeping the area ratio of Ni $2p_{3/2}$ and Ni $2p_{1/2}$ constant at approximately 2. The Ni $2p_{3/2}$ spectrum of the monometallic sample exhibits a main feature peaked at 852.8 eV and a satellite peak at 858.5 eV, which indicates the deposition of a unique phase, composed of metallic Ni [8,33], in good agreement with XRD data. It should be mentioned that, resulting from its interaction with HAP support, the position of the main peak is somewhat shifted towards higher binding energies compared with literature data [33]. Regarding La-promoted samples, the deconvolution of the main feature displays two peaks, centered at 850.9 ± 0.3 eV and at 852.6 ± 0.4 eV, suggesting that the supported Ni species become at least distributed between two distinct sites. Taking the monometallic sample as a reference, we may reasonably assume the existence of an additional Ni phase, exhibiting a certain interaction with lanthana, giving rise to a modification in the electronic properties of Ni, lowering its BE to 850.9 ± 0.3 eV. On the other hand, according to Table 2, an increase in the Ni/P atomic ratio can be observed with La loading increase, which suggests that enrichment of the catalyst surface with La effectively favors a good dispersion of metallic Ni, in consistency with our HAADF studies.

3.1.5. Reducibility of the catalysts

The H$_2$-TPR experiments have been carried out to investigate the reducibility of the supported Ni species. The diagrams of Ni/La-(x) catalysts are shown in Fig. 5. The profile of the HAP support presents two weak reduction peaks, centered at 300 °C and 400 °C, attributed to dehydroxylation of hydroxyapatite [23]. The diagram of Ni/La-(0) sample is dominated by an intense peak, at 345 °C, accompanied by a shoulder at 430 °C. The first feature is assigned to the reduction of surface NiO species (α species), while the second one can be associated with the reduction of NiO presenting a strong interaction with HAP (β species) [23]. Interestingly, the addition of 1% La (Ni/La-(1)) shifts the peaks towards lower temperatures, attesting the promoter effect of lanthanum on the reduction of Ni species. However, no similar effect can be observed in the case of the sample containing 3.7% La (Ni /La-(3.7)). At a higher La content (Ni/La-(6.6)), the reduction process exhibits a complex profile. In this case, three reduction peaks are observed, one of them located at a very low temperature (200 °C). The presence of the latter has few precedents in the available literature. Yakoob et al. [34] observed a similar feature in a Ni/Al$_2$O$_3$ catalyst, attributed to a NiO phase exhibiting a minimal or no interaction with alumina support.

The integration of the H$_2$-TPR profiles indicates that there is a systematic increase in the amounts of consumed H$_2$ with the increase of La content (Table 3). Moreover, irrespective of the La-modified sample, the amounts of H$_2$ are significantly larger than those required for the reduction of a stoichiometric NiO phase (0.55 mmol$_{H2}$ g^{-1}). The observed tendency can be associated with the presence of highly reducible Ni sites, most likely corresponding to those located at the vicinity of the NiO-La$_2$O$_3$ interface. This is in turn consistent with the observed increase in the density of defective metallic Ni crystallites with the La loading increase, as verified by combining HAADF and XRD data for the reduced samples. It is worth outlining that, in contrast to Ni/La/Al$_2$O$_3$ and Ni/La/zeolite reference materials [8,12], our results evidence the promoter effect of La on the reducibility of the Ni/La-(x) catalysts. Thus, it should be highlighted the beneficial effect of the HAP support on the reducibility of the bimetallic Ni-La system.

3.1.6. Temperature programmed desorption of CO$_2$ (CO$_2$-TPD) and temperature programmed surface reaction (TPSR) studies

The surface basicity of the reduced Ni/La-(x) samples has been investigated by means of CO$_2$-TPD techniques. Fig. 6a and Table 3 summarize the obtained results. The density of CO$_2$ desorbed from the bare support, 68.1 μmol$_{CO2}$ g^{-1}, is much smaller than that determined for the monometallic Ni/La-(0) catalyst, 117.1 μmol$_{CO2}$ g^{-1}. However,

Table 3
H$_2$-TPR and CO$_2$-TPD data for the reduced Ni/La-(x) samples.

Sample	H$_2$-TPR			CO$_2$-TPD			TPSR
	Total reducibility, mmol$_{H2}$ g^{-1}	α, %	β, %	Total basicity, µmol$_{CO2}$ g^{-1}	Weak basic sites, µmol$_{CO2}$ g^{-1}	Strong basic sites, µmol$_{CO2}$ g^{-1}	Produced CH$_4$, µmol$_{CH4}$ g^{-1}
HAP	0.21	–	–	68.1	42.2 (61.9%)[a]	25.9 (38.1%)[a]	–
Ni/La-(0)	0.57	76.7	23.3	117.1	80.2 (68.5%)	36.9 (31.5%)	40.4 (34.5%)[b]
Ni/La-(1)	0.70	47.6	52.4	123.2	79.9 (64.9%)	43.2 (35.1%)	61.6 (50.1%)
Ni/La-(3.7)	0.94	66.8	33.2	179.6	89.6 (49.9%)	90.0 (50.1%)	139.0 (77.4%)
Ni/La-(6.6)	1.21	39.9 (26.9)[c]	33.2	222.2	40.4 (18.2%)	181.8 (81.8%)	179.6 (80.8%)

[a] Data corresponding to the relative contribution of the basic sites classified according to their strength nature (weak and strong sites).
[b] Data corresponding to the relative contribution of the active basic sites involved in the methanation (referred to the total amounts of basic sites included in 5th column).
[c] Contribution of the reduction peak at low temperature (200 °C).
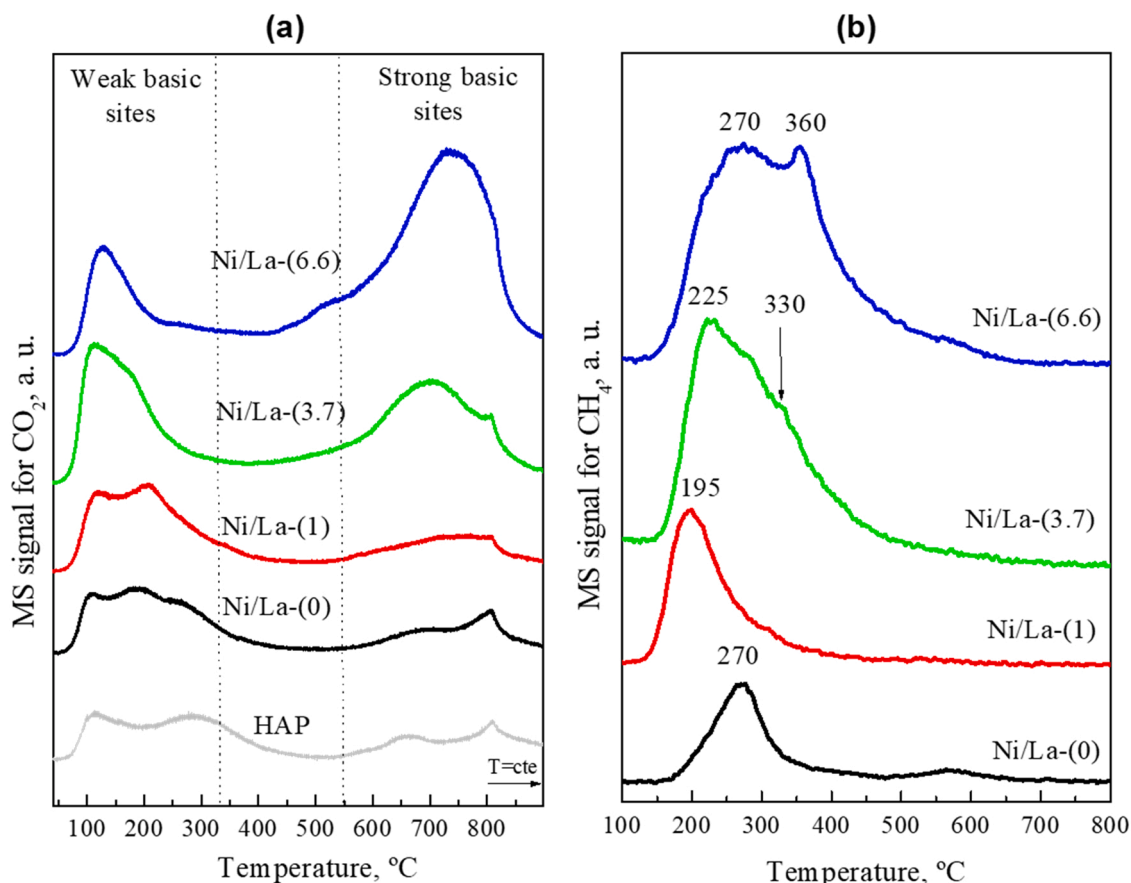
Fig. 6. Diagrams corresponding to (a) CO$_2$-TPD and (b) CH$_4$ formation during TPSR experiments with pre-adsorbed CO$_2$ on the reduced Ni/La-(x) catalysts.

no significant difference is noticed in the distribution of their basic sites. As can be deduced from Table 3, both of them present a large contribution of weak basic sites (61.9% and 68.5%, respectively) and a relatively small fraction of strong basic sites (38.1% and 31.5%, respectively). This distribution seems to be quite similar to that of the Ni sample modified with 1% La. However, the introduction of higher loadings of La ($\geq$ 3.7%) increases dramatically both the amounts and the thermal stability of the basic sites. For instance, the contribution of strong basic sites increases from 35.1% for Ni/La-(1) to 50.1% for Ni/La-(3.7), and to 81.8% for Ni/La-(6.6). According to previous reports, these thermally stable features can be associated with the presence of sub-surface carbonate forms rather than surface species [17,35]. In this sense, deposition of La$_2$O$_3$ species forming sequential thin layers, deduced from our XPS and electron microscopy studies, is fully consistent with the occurrence of a small fraction of strong basic sites in

Ni/La-(1) (vs. the largest fraction found in Ni/La-(6.6)).

In order to assess the reactivity of the basic sites, spread on the reduced catalysts, in the methanation reaction, additional TPSR experiments have been carried out (Fig. 6b and Fig. S4). It should be noted that these experiments consist of a pre-adsorption of CO$_2$ at 100 °C, followed by a heating step under a reducing atmosphere (5% H$_2$/Ar). As it can be deduced from Fig. S4, irrespective of the analyzed sample, the CO$_2$ desorption process only occurs at relatively low temperatures (T < 310 °C, for Ni/La-(0) and T < 250 °C, for La-modified samples). Moreover, in the whole range of the investigated temperatures, no peak due to CO production could be observed (not shown).

Fig. 6b displays the CH$_4$ production profiles for the Ni/La-(x) catalysts. On the unpromoted sample the methane production starts at 175 °C and increases slowly giving rise to a main peak centered at 270 °C. All La-modified samples, however, are activated at lower temperature

(145 °C), but their profiles show a progressive increase in the broadness of their CH_4 production interval with the La loading. In contrast to Ni/La-(1), the Ni/La-(3.7) sample exhibits an asymmetric profile peaked at 225 °C and presenting a shoulder near 330 °C; whereas on the Ni/La-(6.6) sample the CH_4 production feature splits into two intense and well-resolved peaks at 270 and 360 °C. These observations suggest that the hydrogenation process on the La-rich samples (3.7–6.6%) involves two distinct active sites. We speculate that the first forms account for carbonates retained on surface La species, most likely located at the proximity of Ni phases, while those occurring at relatively higher temperatures (330–360 °C) correspond to hardly accessible carbonates retained on sub-surface La species. Thus, the relative abundance of the latter on the samples presenting high La loadings is fully consistent with our HAADF/X-EDS results, commented above.

The quantitative data, reported in Table 3, show that the effect of increasing La loading would mainly consist of an increase in the amounts of the produced CH_4 (from 40.4 μmol_{CH4} g^{-1}, for the Ni/La-(0), to 179.6 μmol_{CH4} g^{-1}, for the Ni/La-(6.6)). Furthermore, there is a notable difference concerning the evolution of the active fraction of basic sites, those involved in the methanation process. The latter

represent only 34.5% of the total basic sites on the unpromoted sample (Ni/La-(0)), but their contribution increases with La addition to reach 50.1%, for Ni/La-(1), 77.4%, for Ni/La-(3.7) and 80.8%, for Ni/La-(6.6) sample. This evolution could be attributed to very subtle nano-structural changes occurring in both Ni and La species. Particularly, the HAADF results showed that the dispersion of Ni particles was improved with La addition, which probably increased the density of the active surface Ni-La interfaces. A direct proof of that, the samples exhibiting a quite similar dispersion of Ni (Ni/La-(3.7) and Ni/La-(6.6)) present a similar fraction of the active basic sites (77.4–80.8%).

3.2. Catalytic performance

3.2.1. Activity in the CO_2 methanation reaction

Fig. 7a and b displays the methanation light-off profiles in terms of CO_2 conversion and selectivity, respectively, over the reduced Ni/La-(x) catalysts. It should be noted that the effect of La addition on the activity of the catalysts was studied by using a previously optimized Ni loading (Fig. S5). Interestingly, all tested catalysts reach the conversion values corresponding to the thermodynamic equilibrium at temperatures lower than 450 °C (Fig. 7a). With reference to the unpromoted sample (Ni/La-(0)), the addition of 1% La leads to a slight improvement in the catalytic performance, since a smooth shift of the activity curve towards lower temperatures is observed. This promoting effect, however, is more pronounced on the samples with higher La contents (Ni/La-(3.7) and Ni/La-(6.6)), where the conversion values reach that of the thermodynamic equilibrium at 400 ºC. Furthermore, the two catalysts prove to be more selective towards CH_4 production (Fig. 7b). For instance, at T > 300 °C they exhibit S_{CH4} values ranging between 94% and 100%.

From Fig. 7 the light-off temperatures corresponding to 50% conversion (T_{50}) have been determined and listed in Table 4. The analysis of these data confirms the systematic improvement of the catalytic activity of the Ni/La-(x) system with the La content increase. Thus, the activity of the assayed catalysts follows this general order: Ni/La-(6.6) > Ni/La-(3.7) > Ni/La-(1) > Ni/La-(0).

The stability test, performed at 350 °C, reveals a robust performance of the optimized Ni/La-(6.6) catalyst (Fig. 8). After activation period of 10 h, it does not present signs of deactivation up to 100 h TOS, reaching a CO_2 conversion close to 73% and a high selectivity towards methane production (> 98%). The observed activation period is consistent with an advantageous re-distribution of the Ni particles which show a decrease in their average size from 8.1 to 7.2 nm (Figs. S6 and S7). In parallel, as it can be deduced from Fig. S8, TGA analysis shows that there is no significant carbon deposition on the spent catalyst. Interestingly, the behavior of our Ni/La-(6.6) sample clearly outperforms that reported over an optimized Ni/La/β-zeolite catalyst assayed at the same temperature (350 °C) [8], which suffered from a significant deactivation process, since CO_2 conversion decreased from 70% to 60% during the initial 24 h TOS.

In order to compare their specific activity, the catalysts were submitted to additional experiments under differential reactor conditions (X_{CO2} < 15%). The absence of mass and heat transport limitations have been assessed according to standard criteria (Table S1 and Table S2).
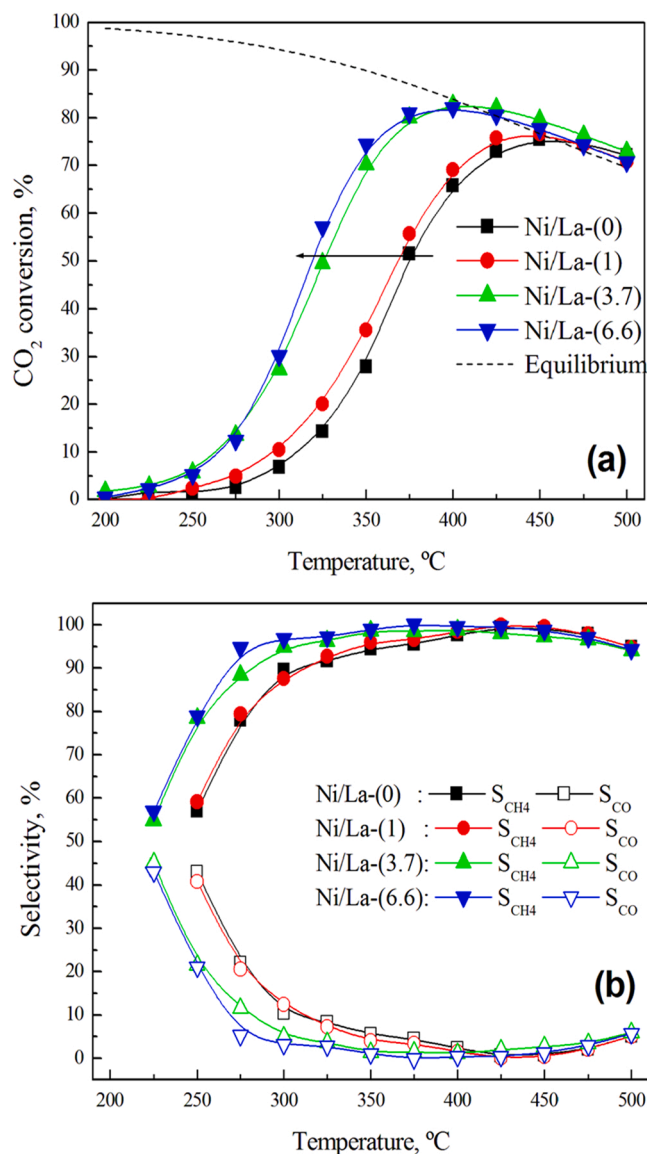

Fig. 7. Catalytic activity of the Ni/La-(x) catalysts in the CO_2 methanation reaction. Reaction mixture conditions: 16% CO_2 and 64% H_2, balanced in He (WHSV = 30,000 cm^3 g^{-1} h^{-1}).

Table 4
Catalytic activity data of the Ni/La-(x) samples in the CO_2 methanation reaction.

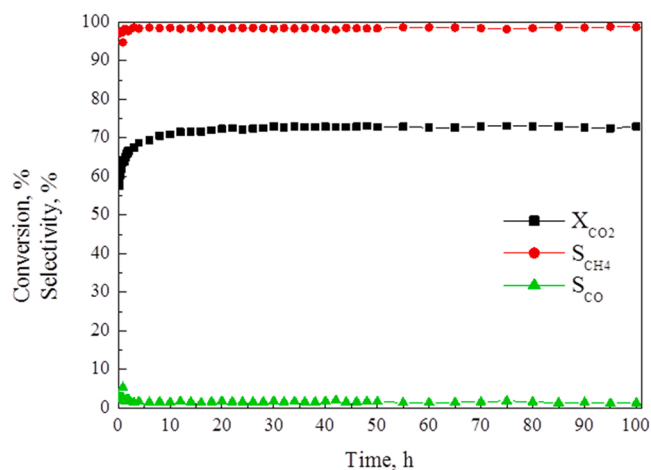| Catalyst	T_{50}, °C	r, mol_{CO2} g^{-1} s^{-1} (350 °C)	TOF, s^{-1} (350 °C)	E_a, kJ mol^{-1} (310–350 °C)
Ni/La-(0)	375	2.4×10^{-5}	1.04	79.2
Ni/La-(1)	367	3.6×10^{-5}	1.07	87.6
Ni/La-(3.7)	327	1.7×10^{-4}	2.06	126
Ni/La-(6.6)	318	2.6×10^{-4}	3.03	128

Fig. 8. Catalytic stability of the Ni/La-(6.6) sample in the methanation reaction, at 350 °C, under 16% CO_2 and 64% H_2, balanced in He (WHSV = 30,000 cm^3 g^{-1} h^{-1}).
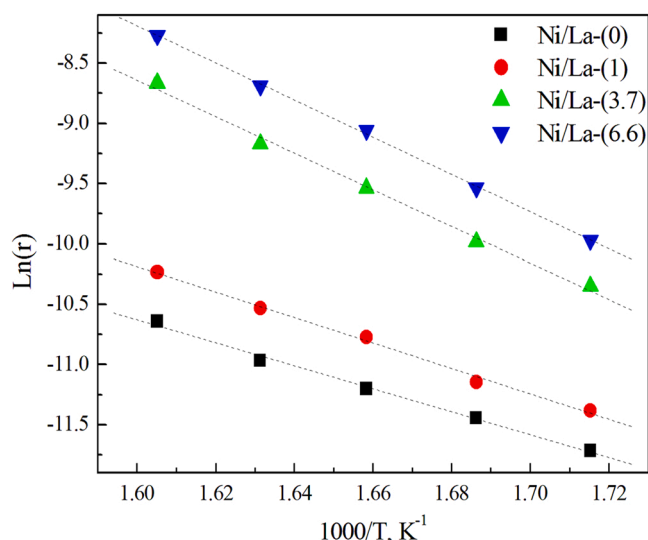

Fig. 9. Arrhenius plots for the reduced Ni/La-(x) catalysts.

Before their testing, they were aged under the reaction mixtures at 500 °C for 2 h. Turnover frequency (TOF) values were calculated, at 350 °C, as the moles of reacted CO_2 per mole of surface Ni, as estimated by electron microscopy (Table 4). The La-rich catalyst (Ni/La-(6.6)) gives the highest TOF value (3.03 s^{-1}) followed by the Ni/La-(3.7) catalyst (2.06 s^{-1}). The unpromoted catalyst, however, presents the poorest specific activity (1.04 s^{-1}), which evidence once again the promoting effect of La on the efficiency of Ni active sites. In good agreement with our nano-analytical studies, these results would imply the dependence of the CO_2 methanation reaction on the Ni particle size. Indeed, the most active catalyst (Ni/La-(6.6)) comprise the smallest Ni particles (8.1 nm), whereas the worst performance is observed over the monometallic catalyst which contains the largest particles (15.3 nm). Our H_2-TPR data also evidenced the improvement of the reducibility of the catalysts with La addition, owing to the occurrence of additional reducible sites on the Ni-La$_2$O$_3$ interface. Thus, these surface defects seem to generate very reactive and dynamic sites. In fact, our CO_2-TPD and TPSR data evidenced the high capacity of the latter to take advantage of a large fraction of the basic sites for the effective methanation of CO_2.

Table 4 also lists the apparent activation energy (E_a) extracted from

Arrhenius plots in the temperature range of 310–350 °C (Fig. 9). Over the monometallic Ni/La-(0) sample the estimated E_a is about 79.2 kJ mol^{-1}. The progressive addition of La systematically increases the E_a values, becoming ranging between 126 and 128 kJ mol^{-1} for the Ni/La-(3.7) and Ni/La-(6.6) catalysts, which agree with those estimated for a number of Ni/Al$_2$O$_3$ catalysts (100–130 kJ mol^{-1}) [36–38]. This evolution suggests that the mechanism pathway depends on the promoter loading. As assessed by CO_2-TPD studies, the surface of Ni/La-(3.7) and Ni/La-(6.6) samples bears the largest amounts of strong basic sites (90 and 181.8 μmol$_{CO2}$ g^{-1}, respectively). It seems that the latter play a determinant role in the activation and the mobility of CO_2 on the catalyst surface. And in an opposite way, the relatively small amounts of strong basic sites spread on the Ni/La-(0) and Ni/La-(1) samples (36.9 and 43.2 μmol$_{CO2}$ g^{-1}, respectively) could explain their lowest E_a values among all investigated samples. In good agreement with earlier studies [8,12], this clearly indicates that the activity of the investigated La-modified Ni catalysts for the methanation reaction can also be correlated with the distribution and the number of basic sites, which are responsible for the CO_2 adsorption.

In order to provide insight into the suitability of our Ni/La-(x) catalysts we compare in Table 5 their performance with those of different Ni catalysts, reported in the literature [8,12,36,39,40]. As can be seen, a variety of supports have been examined, including Al$_2$O$_3$, zeolite and CeO$_2$. In most cases Ni contents higher than 5 wt% were supported on them. We may conclude that, though they contain relatively low Ni loading (3.2 wt%), our optimized catalysts (Ni/La-(3.7) and Ni/La-(6.6)) compete with these reference formulations advantageously. Specially, we can highlight their superiority when compared with the performance achieved over Ni catalysts supported on La-modified β-zeolite support, assayed under similar conditions [8]. Moreover, it is clear that the promoting effect of La on the activity of Ni catalyst is more pronounced for our HAP-based materials, suggesting the suitability of our home-made support for the CO_2 methanation reaction. In this line, it is also worth outlining the superiority of our free-promoter sample (Ni/La-(0)) with respect to 9.5%Ni/Na-zeolite and 4%Ni/Al$_2$O$_3$ catalysts [8,36]. It should be stressed that despite their poor textural properties, the very much improved structural, chemical and catalytic properties of our series of catalysts allow them to represent an advantageous alternative to traditional basic catalytic materials.

3.2.2. Cyclic tests of CO_2 adsorption and methanation experiments

The Ni/La-(x) catalytic materials have also been assayed under cycling CO_2 adsorption and methanation conditions. According to previous reports, implementing this strategy in power generation plants appears to be attractive [2–5]. Its application, for instance, offers the possibility of in-situ recycling the combustion waste gas, taking advantage of residual heat generated.

Fig. 10 shows the variation of the amounts of stored CO_2 and produced CH_4 and CO with the temperature estimated from alternate cycles, including the CO_2 adsorption and methanation period, respectively. To figure out the details of the experiments six CO_2 storage/reduction cycles corresponding to the Ni/La-(6.6) sample, recorded at 400 °C, are included in Fig. S9.

The analysis of the obtained results shows that the progressive addition of the adsorbent onto the HAP surface dramatically increases the amounts of stored CO_2 as well as the released CH_4 and CO products. For instance, at 440 °C, the capacity of the Ni/La-(6.6) catalyst to store CO_2 (84.8 μmol$_{CO2}$ g^{-1}) is more than 2.5 times higher than that measured on the monometallic catalyst (33.3 μmol$_{CO2}$ g^{-1}). A similar trend can be observed in the efficiency of the catalysts to convert the stored CO_2 to methane during the reduction period. These results can be correlated with the observed increase in the number of the surface basic sites, assessed by CO_2-TPD as well as the significant improvement of dispersion of Ni particles. It is important to stress that over the whole investigated temperatures the Ni/La-(6.6) catalyst achieves nearly 100% CO_2 conversion. Zhou et al. [41] associated this behavior with the

Table 5
Comparison of the catalytic performance of Ni/La-(x) catalysts with different Ni catalyst formulations reported in the literature.

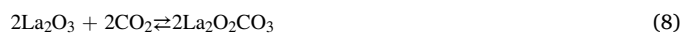| Catalyst	Ni, wt%	Feed gas composition: $CO_2/H_2/He$	WHSV, $cm^3 \, h^{-1} \, g^{-1}$	T_{50}, °C	T_{eq}, °C [a]	Ref.
Ni/La-(0)	3.3			375	450	
Ni/La-(1)	3.2			368	450	This work
Ni/La-(3.7)	3.2	1/4/1.25	30,000	327	400	
Ni/La-(6.6)	3.2			318	400	
Ni/Al$_2$O$_3$	4			440	> 500	
Ni/Al$_2$O$_3$	8			378	> 500	
Ni/Al$_2$O$_3$	12	1/5/1.5	30,000	340	> 500	[36]
Ni/Al$_2$O$_3$	16			329	500	
Ni/Al$_2$O$_3$	20			318	475	
Ni/CeO$_2$	5	1/4/1.25	30,000	357	500	[39]
Ni/Ce$_{0.85}$Zr$_{0.15}$O$_2$	5			337	500	
Ni/β-zeolite	9.5			377	475	
Ni/5La$_2$O$_3$/β-zeolite	9.6	1/4/1.25	30,000	332	475	[8]
Ni/10La$_2$O$_3$/β-zeolite	7.8			322	450	
Ni/15La$_2$O$_3$/β-zeolite	7.3			326	450	
Ni/Ce	10			500	n.d.	
Ni/Sm-Ce	10	1/4/5	25,000	390	n.d.	[40]
Ni/Pr-Ce	10			340	n.d.	
Ni-Mg-Ce	10			390	n.d.	
Ni/Al$_2$O$_3$	13.6			340	450	
Ni/4La$_2$O$_3$/Al$_2$O$_3$	13.6	1/5/10.7	54,420	330	450	[12]
Ni/14La$_2$O$_3$/Al$_2$O$_3$	13.6			300	400	
Ni/37La$_2$O$_3$/Al$_2$O$_3$	13.6			330	450	
10%LaNiO$_3$/CeO$_2$	2.8	1/4/1.25	30,000	312	500	[47]

Temperature at which the catalyst reaches the thermodynamic equilibrium.
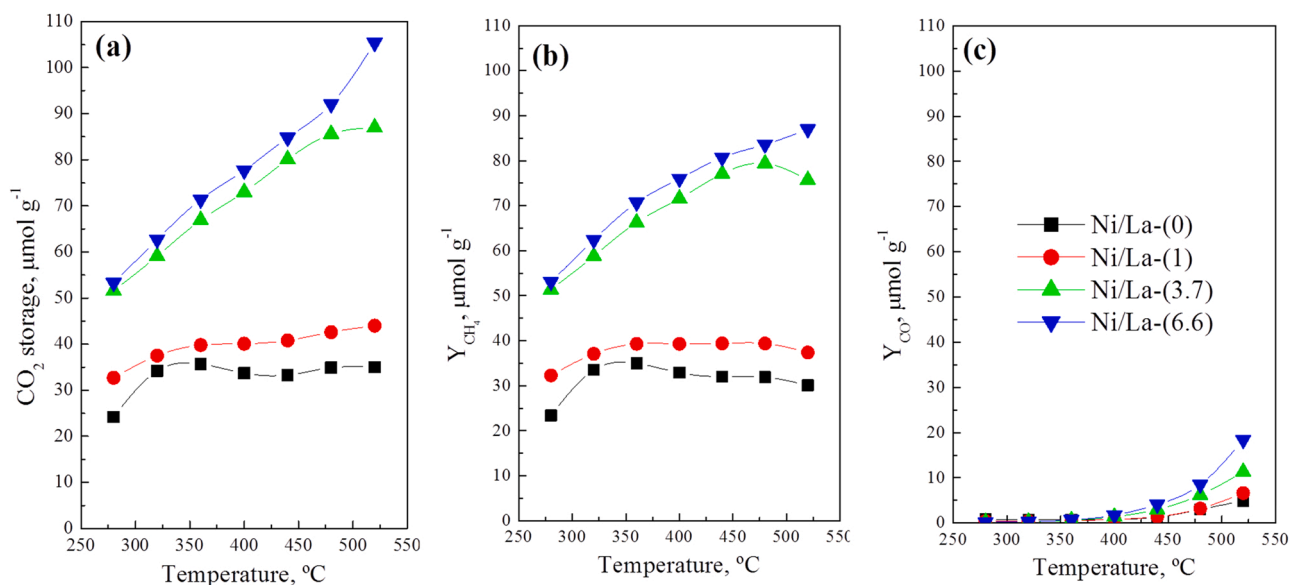
Fig. 10. Evolution of (a) CO_2 storage and production of (b) CH_4 and (c) CO versus the temperature of the cycling CO_2 storage/reduction process.

formation of very reactive carbonate species. In this sense, we think that the interaction between Ni and La phases maximizes the spillover of CO_2 from the adsorbent to the active Ni sites. In addition, over the most active catalyst (Ni/La-(6.6)) the density of captured CO_2 and the CH_4 and CO yields increase continuously with the rise of temperature to reach values close to 105, 87 and 18.4 μmol g^{-1}, respectively, at 520 °C. Bermejo-López et al. [30] observed a similar behavior over Ni/CaO/Al$_2$O$_3$ DFM samples and explained this tendency with the increase of temperature by promotion of the ability of the catalyst to regenerate CO_2 adsorption sites, which increases the CO_2 storage capacity. This dynamic behavior, generating surface reactivity, seems to determine the activity in the posterior methanation period. Thus, the behavior of the catalyst mainly depends on the nature of CO_2 adsorption sites that are assumed to be involved. The similarity observed in the evolution of the activity of our Ni/La/HAP catalyst compared with that

of Ni/CaO/Al$_2$O$_3$ can be explained by a similar distribution of the basic sites. In fact, as in the case of our DFM, the Ni/CaO/Al$_2$O$_3$ mainly provided strong basic sites. By contrast, the shape of the activity of Ni/Na$_2$O$_3$/Al$_2$O$_3$ DFMs, presenting large density of medium-strength basic sites, exhibited volcano-type curves with reaction temperature, decreasing sharply for T ≥ 340 °C [10,30].

Fig. 11a and b illustrates the evolution of the recorded concentrations of CO_2, CO, H_2O and CH_4 during cycling CO_2 capture and methanation, over the Ni/La-(3.7) and Ni/La-(6.6) samples. It is known that, during the storage period, the adsorption of CO_2 process mainly occurs over lanthana (La$_2$O$_3$) and lanthanum hydroxide (La(OH)$_3$) species leading to their carbonatation, forming lanthanum dioxycarbonate (La$_2$O$_2$CO$_3$) (Eqs. (8) and (9)) [42].
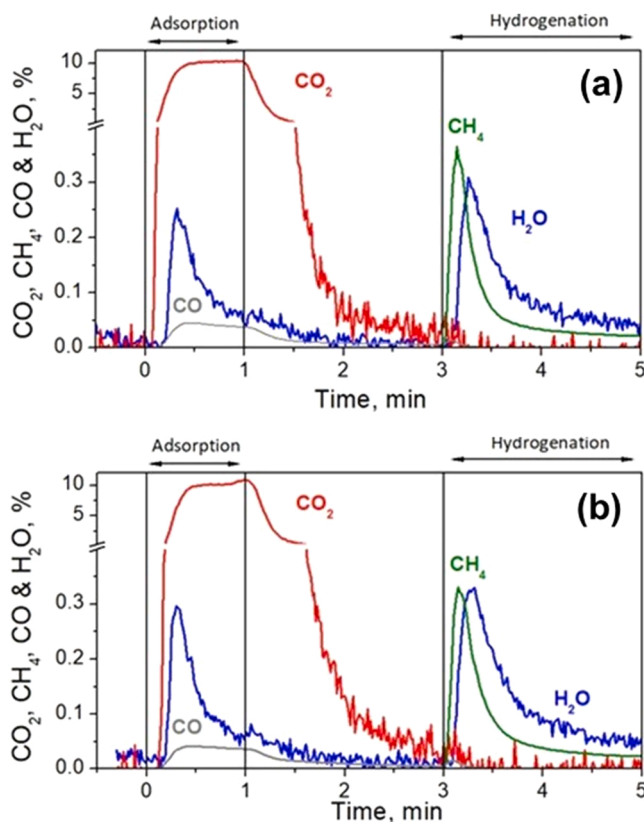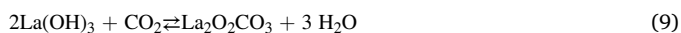
$$2La_2O_3 + 2CO_2 \rightleftarrows 2La_2O_2CO_3 \tag{8}$$

Fig. 11. Profiles of CO_2, CH_4, CO and H_2O concentrations recorded at 400 ºC during one cycle, including CO_2 adsorption (1 min) followed by a hydrogenation period (2 min), for (a) Ni/La-(3.7) and (b) Ni/La-(6.6) DFM materials.

$$3La_2O_2CO_3 \rightleftarrows 3La_2O_3 + 3CO_2 \tag{13}$$

$$3CO_2 + 12\,H_2 \rightleftarrows 3CH_4 + 6\,H_2O \tag{14}$$

$$0{\cdot}5La_2O_3 + 1{\cdot}5\,H_2O \rightleftarrows La(OH)_3 \tag{15}$$

In order to study the limitations of our optimized DFM (Ni/La-(6.6)), the effect of O_2 addition on its performance has also been examined at 440 ºC. As shown in Fig. S10, the addition of O_2 lowers significantly the CH_4 production by around 27% (from 82.3 to 60.4 μmol_{CH4} g^{-1}), due to the oxidation of the Ni active sites [48,49]. In parallel, this increases the amounts of produced CO from 3.3 to 7.3 μmol_{CO} g^{-1}. Nevertheless, the extent of CH_4 selectivity loss is not so profound, since it decreases by 7.3% only (from 96% to 89%). A similar behavior was reported by Kosaka et al. [48] in their study on a Ni-Na/Al_2O_3 DFM. Interestingly, when O_2 flow is stopped, the Ni/La-(6.6) sample tends to recover its activity shown in the absence of O_2, thus indicating the reversibility of its deactivation process.

4. Conclusions

The behavior of a series of nickel supported on lanthana-modified HAP catalysts has been investigated in the CO_2 methanation reaction. A special attention has been paid to the study of the influence of lanthanum loading on their physicochemical and catalytic properties.

The HAADF and XPS results show that there was no apparent segregation of the lanthanum phases in the range of La loadings used in this work (1–6.6 wt%). Instead, we suggest that the surface enrichment of the Ni/La-(x) catalysts with La is rather a stepwise process, following a sequential multilayer deposition model. Moreover, the introduction of La seems to improve the dispersion of Ni particles and their reducibility. In parallel, as deduced from CO_2-TPD and TPSR studies, the progressive addition of La induces significant modifications of the surface basicity as well as its reactivity for CO_2 methanation. On one hand, addition of La increases significantly both the amounts and the thermal stability of basic sites; on the other hand, it increases the active fraction of basic sites involved in the methanation process.

In the CO_2 methanation reaction, the performance of investigated Ni catalysts is systematically enhanced with the increase of La loading. The highest TOF value estimated for La-rich catalysts was explained by the high efficiency of their smallest Ni particles, owing to an increase in the density of surface defects on the Ni-La_2O_3 interface. The long-term stability test at 350 °C, performed on the optimized catalyst, Ni/La-(6.6), evidences its strong resistance to deactivation and high selectivity to methane production, for a prolonged TOS (100 h). The advantages of dispersing the bimetallic Ni-La system on the HAP support are fully confirmed by comparison of the performance in the methanation reaction with some reference materials (zeolite, ceria and alumina-based catalysts). The improved physicochemical properties of our novel materials seems to compensate their poor textural properties. Moreover, our formulation offers the possibility of working with relatively lower Ni and La loadings (3.2 and 6.6 wt%, respectively).

The investigated Ni/La-(x) samples have also been tested as DFMs for CO_2 capture and methanation. Over the most active DFM (Ni/La-(6.6)) the density of captured CO_2 and CH_4 yield continuously increase with the rise of temperature to reach values close to 105 and 87 μmol g^{-1}, respectively, at 520 °C. This behavior with temperature is associated with the nature of CO_2 adsorption sites (weak and strong basic sites) that are assumed to be involved.

A scheme is proposed to describe the different steps involved in a CO_2 adsorption/hydrogenation cycle. It is found that the distribution of CH_4, CO and H_2O products mainly depends on the ability of lanthanum phases to undergo a series of chemical transformations facilitating their carbonatation/decarbonation process. It should be highlighted that, in contrast to a number of Ni-based DFMs, over our Ni/La-(x) formulation the methanation period does not yield significant amounts of CO. This is

$$2La(OH)_3 + CO_2 \rightleftarrows La_2O_2CO_3 + 3\,H_2O \tag{9}$$

The presence of relatively small amounts of CO in the carbonatation period can be associated with the reverse water-gas shift reaction (RWGS) (Eq. (10)), which probably involves the chemisorbed H_2 on Ni active sites, under the previous hydrogenation period conditions [30]. Instead, some reports also suggested the formation of lanthanum hydroxycarbonate (La(OH)CO_3) phase intermediate species when $La_2O_2CO_3$ was exposed to H_2O and CO_2 (Eq. (11)) [43–45]. This possibility cannot be ruled out, since this intermediate could decompose to relatively stable carbonates ($La_2O_2CO_3$), producing CO and surface hydroxyl groups (OH*), according to Eq. (12).

$$H_2 + CO_2 \rightleftarrows CO + H_2O \tag{10}$$

$$La_2O_2CO_3 + H_2O + CO_2 \rightleftarrows 2La(OH)CO_3 \tag{11}$$

$$2La(OH)CO_3 \rightleftarrows La_2O_2CO_3 + CO + 2OH^* \tag{12}$$

Feeding H_2 during the methanation period favors the decomposition of carbonates (Eq. (13)) and the subsequent spillover of CO_2 to Ni active sites, before its reaction with hydrogen to produce methane and water (Eq. (14)). Note that the H_2O/CH_4 ratio calculated for the hydrogenation period (~1.5) is significantly lower than that of a stoichiometric methanation reaction (2). Generally, this behavior agrees with the hydration process of the used adsorbent [30]. Hydration of lanthana produces its corresponding hydroxide, La(OH)$_3$, according to Eq. (15). It should be highlighted that, in contrast to a number of Ni-based DFMs [30], over our Ni/La-(x) formulation the methanation period does not yield significant amounts of CO. This behavior could be linked to the moderate acidity of the HAP support, which does not favor the RWGS reaction [46].

explained by the moderate acidity of the HAP support, which does not favor the occurrence of the RWGS reaction.

Credit author statement

Zouhair Boukha: Conceptualization, Investigation, Methodology, Software, Data curation, Writing – original draft, Funding acquisition. **Alejandro Bermejo-López:** Investigation, Methodology, Software, Data curation. **Beñat Pereda-Ayo:** Funding acquisition. **José A. González-Marcos:** Funding acquisition. **Juan R. González-Velasco:** Conceptualization, Reviewing, Funding acquisition.

Declaration of Competing Interest

The authors declare that they have no known competing financial interests or personal relationships that could have appeared to influence the work reported in this paper.

Acknowledgements

Appendix A. Supporting information

Supplementary data associated with this article can be found in the online version at doi:10.1016/j.apcatb.2022.121500.

References

[1] G. Taylor, S. Vink, Managing the risks of missing international climate targets, Clim. Risk Manag. 34 (2021), 100379.

[2] S. Sun, H. Sun, P.T. Williams, C. Wu, Recent advances in integrated CO_2 capture and utilization: a review, Sustain. Energy Fuels 5 (2021) 4546–4559.

[3] A.I. Tsiotsias, N.D. Charisiou, I.V. Yentekakis, M.A. Goula, The role of alkali and alkaline earth metals in the CO_2 methanation reaction and the combined capture and methanation of CO_2, Catalysts 10 (2020).

[4] I.S. Omodolor, H.O. Otor, J.A. Andonegui, B.J. Allen, A.C. Alba-Rubio, Dual-function materials for CO_2 capture and conversion: a review, Ind. Eng. Chem. Res. 59 (2020) 17612–17631.

[5] P.M. Bravo, D.P. Debecker, Combining CO_2 capture and catalytic conversion to methane, Waste Dispos. Sustain. Energy 1 (2019) 53–65.

[6] S.B. Walker, D. van Lanen, U. Mukherjee, M. Fowler, Greenhouse gas emissions reductions from applications of Power-to-Gas in power generation, Sustain. Energ. Technol. Assess. 20 (2017) 25–32.

[7] D. Hidalgo, J.M. Martín-Marroquín, Power-to-methane, coupling CO_2 capture with fuel production: an overview, Renew. Sust. Energ. Rev. 132 (2020), 110057.

[8] A. Quindimil, U. De-La-Torre, B. Pereda-Ayo, J.A. González-Marcos, J.R. González-Velasco, Ni catalysts with La as promoter supported over Y- and BETA- zeolites for CO_2 methanation, Appl. Catal. B-Environ. 238 (2018) 393–403.

[9] S.T. Yang, J. Kim, W.S. Ahn, CO_2 adsorption over ion-exchanged zeolite beta with alkali and alkaline earth metal ions, Microporous Mesoporous Mater. 135 (2010) 90–94.

[10] P. Hongmanorom, J. Ashok, G. Zhang, Z. Bian, M.H. Wai, Y. Zeng, S. Xi, A. Borgna, S. Kawi, Enhanced performance and selectivity of CO_2 methanation over phyllosilicate structure derived Ni-Mg/SBA-15 catalysts, Appl. Catal. B-Environ. 282 (2021), 119564.

[11] D. Wierzbicki, R. Debek, M. Motak, T. Grzybek, M.E. Gálvez, P. Da Costa, Novel Ni-La-hydrotalcite derived catalysts for CO_2 methanation, Catal. Commun. 83 (2016) 5–8.

[12] G. Garbarino, C. Wang, T. Cavattoni, E. Finocchio, P. Riani, M. Flytzani-Stephanopoulos, G. Busca, A study of Ni/La-Al$_2$O$_3$ catalysts: a competitive system for CO_2 methanation, Appl. Catal. B-Environ. 248 (2019) 286–297.

[13] P. Riani, I. Valsamakis, T. Cavattoni, V. Sanchez Escribano, G. Busca, G. Garbarino, Ni/SiO$_2$-Al$_2$O$_3$ catalysts for CO_2 methanation: effect of La$_2$O$_3$ addition, Appl. Catal. B-Environ. 284 (2021), 119697.

[14] T. Burger, P. Donaubauer, O. Hinrichsen, On the kinetics of the co-methanation of CO and CO_2 on a co-precipitated Ni-Al catalyst, Appl. Catal. B-Environ. 282 (2021), 119408.

[15] C. Italiano, G.D. Ferrante, L. Pino, M. Laganà, M. Ferraro, V. Antonucci, A. Vita, Silicon carbide and alumina open-cell foams activated by Ni/CeO$_2$-ZrO$_2$ catalyst for CO_2 methanation in a heat-exchanger reactor, Chem. Eng. J. 434 (2022), 134685.

[16] W. Ahmad, M.N. Younis, R. Shawabkeh, S. Ahmed, Synthesis of lanthanide series (La, Ce, Pr, Eu & Gd) promoted Ni/γ-Al2O3 catalysts for methanation of CO_2 at low temperature under atmospheric pressure, Catal. Commun. 100 (2017) 121–126.

[17] Z. Boukha, L. Fitian, M. López-Haro, M. Mora, J.R. Ruiz, C. Jiménez-Sanchidrián, G. Blanco, J.J. Calvino, G.A. Cifredo, S. Trasobares, S. Bernal, Influence of the calcination temperature on the nano-structural properties, surface basicity, and catalytic behavior of alumina-supported lanthana samples, J. Catal. 272 (2010) 121–130.

[18] G.I. Siakavelas, N.D. Charisiou, A. AlKhoori, S. AlKhoori, V. Sebastian, S.J. Hinder, M.A. Baker, I.V. Yentekakis, K. Polychronopoulou, M.A. Goula, Highly selective and stable Ni/La-M (M=Sm, Pr, and Mg)-CeO$_2$ catalysts for CO_2 methanation, J. CO_2 Util. 51 (2021), 101618.

[19] Z. Boukha, J.R. González-Velasco, M.A. Gutiérrez-Ortiz, Platinum supported on lanthana-modified hydroxyapatite samples for realistic WGS conditions: on the nature of the active species, kinetic aspects and the resistance to shut-down/start-up cycles, Appl. Catal. B-Environ. 270 (2020), 118851.

[20] Z. Boukha, J.R. González-Velasco, M.A. Gutiérrez-Ortiz, Exceptional performance of gold supported on fluoridated hydroxyapatite catalysts in CO-cleanup of H$_2$-rich stream: High activity and resistance under PEMFC operation conditions, Appl. Catal. B-Environ. 292 (2021), 120142.

[21] M.H. Wai, J. Ashok, N. Dewangan, S. Das, S. Xi, A. Borgna, S. Kawi, Influence of surface formate species on methane selectivity for carbon dioxide methanation over nickel hydroxyapatite catalyst, ChemCatChem 12 (2020) 6410–6419.

[22] X.- Pham, U.P.M. Ashik, J.- Hayashi, A. Pérez Alonso, D. Pla, M. Gómez, D. Pham Minh, Review on the catalytic tri-reforming of methane - part II: catalyst development, Appl. Catal. A-Gen. 623 (2021), 118286.

[23] Z. Boukha, M.P. Yeste, M.Á. Cauqui, J.R. González-Velasco, Influence of Ca/P ratio on the catalytic performance of Ni/hydroxyapatite samples in dry reforming of methane, Appl. Catal. A-Gen. 580 (2019) 34–45.

[24] Z. Boukha, J.L. Ayastuy, M. Cortés-Reyes, L.J. Alemany, J.R. González-Velasco, M.A. Gutiérrez-Ortiz, Catalytic performance of Cu/hydroxyapatite catalysts in CO preferential oxidation in H$_2$-rich stream, Int. J. Hydrog. Energ. 44 (2019) 12649–12660.

[25] K. Ishisone, N. Jiraborvornpongsa, T. Isobe, S. Matsushita, M. Wakumura, M. Oshikiri, A. Nakajima, Experimental and theoretical investigation of WOx modification effects on the photocatalytic activity of titanium-substituted hydroxyapatite, Appl. Catal. B-Environ. 264 (2020), 118516.

[26] H. Yan, S. Yao, T. Zhang, D. Li, X. Tang, M. Chen, Y. Zhou, M. Zhang, Y. Liu, X. Zhou, X. Feng, X. Chen, C. Yang, Promoting catalytic transfer hydrodecarbonylation of methyl stearate over bimetallic CoNi/HAP catalysts with strong electronic coupling effect, Appl. Catal. B-Environ. 306 (2022), 121138.

[27] Z. Boukha, J. González-Prior, B. de Rivas, J.R. González-Velasco, R. López-Fonseca, J.I. Gutiérrez-Ortiz, Pd supported catalyst for gas-phase 1,2-dichloroethane abatement: efficiency and high selectivity towards oxygenated products, J. Ind. Eng. Chem. 57 (2018) 77–88.

[28] A. Bermejo-López, B. Pereda-Ayo, J.A. González-Marcos, J.R. González-Velasco, Mechanism of the CO_2 storage and in situ hydrogenation to CH4. Temperature and adsorbent loading effects over Ru-CaO/Al2O3 and Ru-Na2CO3/Al2O3 catalysts, Appl. Catal. B-Environ. 256 (2019), 117845.

[29] A. Bermejo-López, B. Pereda-Ayo, J.A. González-Marcos, J.R. González-Velasco, Modeling the CO_2 capture and in situ conversion to CH$_4$ on dual function Ru-Na$_2$CO$_3$/Al$_2$O$_3$ catalyst, J. CO_2 Util. 42 (2020), 101351.

[30] A. Bermejo-López, B. Pereda-Ayo, J.A. González-Marcos, J.R. González-Velasco, Ni loading effects on dual function materials for capture and in-situ conversion of CO_2 to CH$_4$ using CaO or Na$_2$CO$_3$, J. CO_2 Util. 34 (2019) 576–587.

[31] J.I. Langford, A.J.C. Wilson, Scherrer after sixty years: a survey and some new results in the determination of crystallite size, J. Appl. Crystallogr. 11 (1978) 102–113.

[32] E.R. Shaaban, M. El-Hagary, E.S. Moustafa, H.S. Hassan, Y.A.M. Ismail, M. Emam-Ismail, A.S. Ali, Structural, linear and nonlinear optical properties of co-doped ZnO thin films, Appl. Phys. A-Mater. 122 (2016) 1–10.

[33] A.M. Hengne, A.K. Samal, L.R. Enakonda, M. Harb, L.E. Gevers, D.H. Anjum, Ni-Sn-supported ZrO$_2$ catalysts modified by indium for selective CO_2 hydrogenation to methanol, ACS Omega 3 (2018) 3688–3701.

[34] Z. Yaakob, A. Bshish, A. Ebshish, S.M. Tasirin, F.H. Alhasan, Hydrogen production by steam reforming of ethanol over nickel catalysts supported on sol gel made alumina: influence of calcination temperature on supports, Materials 6 (2013) 2229–2239.

[35] S. Sato, R. Takahashi, M. Kobune, H. Gotoh, Basic properties of rare earth oxides, Appl. Catal. A-Gen. 356 (2009) 57–63.

[36] A. Quindimil, U. De-La-Torre, B. Pereda-Ayo, A. Davó-Quiñonero, E. Bailón-García, D. Lozano-Castelló, J.A. González-Marcos, A. Bueno-López, J.R. González-Velasco, Effect of metal loading on the CO_2 methanation: a comparison between alumina supported Ni and Ru catalysts, Catal. Today 356 (2020) 419–432.

[37] C.V. Miguel, A. Mendes, L.M. Madeira, Intrinsic kinetics of CO_2 methanation over an industrial nickel-based catalyst, J. CO_2 Util. 25 (2018) 128–136.

[38] T. Van Herwijnen, H. Van Doesburg, W.A. De Jong, Kinetics of the methanation of CO and CO_2 on a nickel catalyst, J. Catal. 28 (1973) 391–402.

[39] I. Iglesias, A. Quindimil, F. Mariño, U. De-La-Torre, J.R. González-Velasco, Zr promotion effect in CO_2 methanation over ceria supported nickel catalysts, Int. J. Hydrog. Energ. 44 (2019) 1710–1719.

[40] G.I. Siakavelas, N.D. Charisiou, S. AlKhoori, A.A. AlKhoori, V. Sebastian, S.J. Hinder, M.A. Baker, I.V. Yentekakis, K. Polychronopoulou, M.A. Goula, Highly selective and stable nickel catalysts supported on ceria promoted with Sm$_2$O$_3$, Pr$_2$O$_3$ and MgO for the CO_2 methanation reaction, Appl. Catal. B-Environ. 282 (2021), 119562.

[41] Z. Zhou, N. Sun, B. Wang, Z. Han, S. Cao, D. Hu, T. Zhu, Q. Shen, W. Wei, 2D-layered Ni-MgO-Al$_2$O$_3$ nanosheets for integrated capture and methanation of CO$_2$, ChemSusChem 13 (2020) 360–368.

[42] T.J. Toops, A.B. Walters, M.A. Vannice, The effect of CO$_2$ and H$_2$O on the kinetics of NO reduction by CH$_4$ over a La$_2$O$_3$/γ-Al$_2$O$_3$ catalyst, J. Catal. 214 (2003) 292–307.

[43] S. Bernal, J.A. Díaz, R. García, J.M. Rodriguez-Izquierdo, Study of some aspects of the reactivity of La$_2$O$_3$ with CO$_2$ and H$_2$O, J. Mater. Sci. 20 (1985) 537–541.

[44] B. Bakiz, F. Guinneton, M. Arab, A. Benlhachemi, S. Villain, P. Satre, J.- Gavarri, Carbonatation and decarbonatation kinetics in the La$_2$O$_3$-La$_2$O$_2$CO$_3$ system under CO$_2$ gas flows, Adv. Mater. Sci. Eng. 2010 (2010), 360597.

[45] S. Valange, A. Beauchaud, J. Barrault, Z. Gabelica, M. Daturi, F. Can, Lanthanum oxides for the selective synthesis of phytosterol esters: correlation between catalytic and acid-base properties, J. Catal. 251 (2007) 113–122.

[46] H. Sakurai, S. Tsubota, M. Haruta, Hydrogenation of CO$_2$ over gold supported on metal oxides, Appl. Catal. A-Gen. 102 (1993) 125–136.

[47] J.A. Onurbia-Calvo, B. Pereda-Ayo, J.A. González-Marcos, A. Bueno-López, J. R. González-Velasco, Design of CeO$_2$-supported LaNiO$_3$ perovskites as precursors of highly active catalysts for CO$_2$ methanation, Catal. Sci. Technol. 11 (2021) 6065–6079.

[48] F. Kosaka, Y. Liu, S.- Chen, T. Mochizuki, H. Takagi, A. Urakawa, K. Kuramoto, Enhanced activity of integrated CO$_2$ capture and reduction to CH$_4$ under pressurized conditions toward atmospheric CO$_2$ utilization, ACS Sust. Chem. Eng. 9 (2021) 3452–3463.

[49] M.A. Arellano-Treviño, Z. He, M.C. Libby, R.J. Farrauto, Catalysts and adsorbents for CO$_2$ capture and conversion with dual function materials: limitations of Ni-containing DFMs for flue gas applications, J. CO2 Util. 31 (2019) 143–151.